Journal of Colloid and Interface Science 635 (2023) 336–347

Contents lists available at ScienceDirect

Journal of Colloid and Interface Science

journal homepage: www.elsevier.com/locate/jcis

Two dimensional $MnPSe_3$ layer stacking composites with superior storage performance for alkali metal-ion batteries

Yan-Fu Huang, Yi-Chun Yang, Yen-Yang Tseng, Hsing-Yu Tuan *

Department of Chemical Engineering, National Tsing Hua University, Hsinchu 30013, Taiwan

GRAPHICAL ABSTRACT

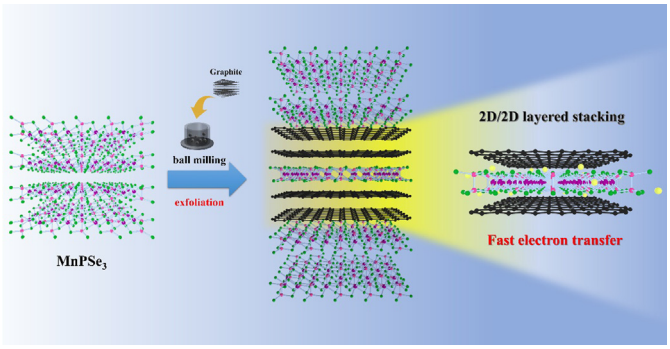

ARTICLE INFO

Article history:
Received 30 October 2022
Revised 7 December 2022
Accepted 18 December 2022
Available online 23 December 2022

Keywords:
Ternary metal phosphorus trichalcogenides
Lithium-ion batteries
Potassium-ion batteries

ABSTRACT

Two-dimensional $MnPSe_3$ Van der Waals stacked in an ABC sequence has abundant and low-cost Mn resources, but has yet to exhibit expected performance as an electrode material in battery devices. Here, we report a 2D/2D composite consisting of few layer $MnPSe_3$ nanosheets and graphite through a high energy ball milling method for uses on the anodes alkali metal-ion batteries, including lithium ion battery (LIB) and potassium ion battery (PIB). These unique 2D/2D layer nanostructures, with $MnPSe_3$ layers hierarchically stacked in graphite, can successfully overcome the severe aggregation due to restacking during charge/discharge cycles. Moreover, density functional theory (DFT) calculations show that the band gap of the $MnPSe_3$/graphite hybrid is as low as 0.07 eV, confirming that the combination of $MnPSe_3$ and graphite efficiently reduces the ion migration energy barrier. As a result, $MnPSe_3$/graphite stacking composites achieve a discharge capacity of 488.1 mA h g^{-1} after 500 cycles at 2000 mA g^{-1} in LIB, and 236.7 mA h g^{-1} after 700 cycles at 250 mA g^{-1} in PIB. Moreover, the analysis of electrochemical, kinetics, reactions mechanism, DFT, and full cell applications were investigated deeply. This work strongly supports the possibility of $MnPSe_3$/graphite hybrid as a promising candidate for alkali ion batteries, and makes important improvements for the application of two-dimensional $MPCh_3$ layer materials in storage systems.

1. Introduction

With the excessive dependence on fossil energy, it is urgent to develop high-energy storage systems to satisfy the increasing energy demand [1,2]. For the metal-ion batteries field, lithium-

* Corresponding author.
E-mail address: hytuan@che.nthu.edu.tw (H.-Y. Tuan).

https://doi.org/10.1016/j.jcis.2022.12.082
0021-9797/

ion batteries (LIBs) have been widely used in storage equipment and developing rapidly due to high energy density, high operating voltage, and long cycle life [3–6]. However, the shortage and uneven global distribution of lithium resources limit large-scale energy storage applications and the development of electric vehicle technology in the future [7–9]. Recently, many studies have explored other metal ions batteries as alternatives for LIB. Among them, potassium-ion batteries (PIBs) are considered as potential candidates owing to the abundant K resources and low cost [10–13]. In addition, both of the elements Li and K belong to the same group (group IA) of the periodic table, so the development and advancement of LIBs can provide a reference for the research field of PIBs [14–16]. Unfortunately, it remains a considerable challenge to explore the suitable electrode materials for various alkali metal ions (Li^+ or K^+) because both of the ionic radius (Li^+ = 0.76 Å, K^+ = 1.38 Å) and battery systems are different [17,18].

Given the urgent requirement for reliable materials in the field of energy storage, two-dimensional (2D) materials have attracted great attention, such as graphene [19], transition metal dichalcogenides [20], black phosphorus [21], etc. The unique structural property shortens ion diffusion distances and the high specific surface area provides a large number of active sites for ion storage [22–25]. Among 2D materials, the transition metal phosphorus trichalcogenide ($MPCh_3$, M = Co, Mn, Fe, Ni and Ch = S, Se) is cost-effective and easily available material. The $MPCh_3$ layers with metal cations (M^{2+}) and $[P_2Ch_6]^{4-}$anions are stacked by van der Waals interactions [26,27]. Compared with 2D P-based or S/Se-based binary materials, $MPCh_3$ has a more complex microstructure and adjustable electronic states. $MPCh_3$ as anode for energy storage system has been gradually reported [28], for example, Ma *et al.* reported that few-layer $FePS_3$ nanosheets modified by *N*-doped carbon exhibit a superior cycling performance for 800 cycles [28]. Yang *et al.* prepared the $Cd_{1-x}PS_3Li_{2x}$ electrode with high capacities of 1056 mA h g^{-1} at 0.2 A g^{-1} and 678 mA h g^{-1} at 8 A g^{-1} for LIBs, showing the excellent electrochemical performance [29]. However, $MPCh_3$ still has some shortcomings for practical applications, such as agglomeration, dramatic volume changes between adjacent layers, further resulting in poor electrochemical performance.

It is difficult to directly use raw materials as electrodes to achieve excellent electrochemical performance. Therefore, it has been reported that synergistic effects between two or more materials have been designed to combine the advantages of each material, thereby improving the structural stability of 2D materials [30]. In terms of operation complexity and low cost, carbon hybrid composites are regarded as a most efficient strategy to improve the performance of 2D materials. Due to its flexible and conductive properties, carbon can act as a buffer layer to effectively accommodate the large volume change during the ion interaction/extraction process, and significantly enhance electron transfer [31–33]. Recently, carbon nanotubes (CNTs) are considered as ideal additive materials to improve the electrochemical properties of the electrode for metal-ion batteries due to their unique one-dimensional tubular structure, high electrical and thermal conductivity, and extremely large surface area [34–36]. Kim *et al.* reported a $Sn_2P_2S_6$-CNT heterostructure based on the Mott–Schottky concept, the built-in electric field promotes the ion extraction during the charging process and improves the stability of the SEI layer [37]. On the other hand, graphene is also an attractive candidate due to its unique single-atom-layer structure with superior mechanical properties and high electron mobility. Lu *et al.* synthesized a novel 2D/2D $SnSe_2$/graphene heterostructure with an interface coupling effect. The chemically coupled bond between graphene and $SnSe_2$ nanosheets can prevent the agglomeration of nanosheets and improve the cycle stability [38]. However, insufficient coupling between different materials may affect the high-speed charge transfer kinetics, resulting in large charge transfer resistance during the charge and discharge process [39]. Therefore, a simple and efficient synthetic strategy is required to construct the perfect coupled heterostructures.

Manganese (Mn) is a rock-forming element. Although Mn is abundant resources and low cost, most Mn-based anodes exhibit poor electrochemical performance due to poor electrical conductivity. In this work, we constructed a novel 2D/2D $MnPSe_3$/graphite hybrid as an anode for LIBs and PIBs. Through one-step high-energy ball milling (HEBM), the graphite with a good electrical conductor is stacked on the $MnPSe_3$ nanosheets to further enhance the electron transport and effectively reduce the aggregation of $MnPSe_3$ nanosheets during the charging and discharging process (Scheme 1). The $MnPSe_3$/graphite hybrid delivers 488.1 mA h g^{-1} at 2 A g^{-1} for LIB and 236.7 mA h g^{-1} at 0.25 A g^{-1} for PIB, and, the $MnPSe_3$/graphite anode exhibits high rate (194.4 mA h g-1, 10 A/g) for LIBs. As revealed by density functional theory (DFT) calculations as show that the bulk $MnPSe_3$ has been discovered as a semiconductor with a large band gap of 1.72 eV, resulting in the relatively poor conductivity and slow electron transfer. Conversely, the band gap of the $MnPSe_3$/graphite hybrid declines significantly to 0.07 eV, confirming that the combination of $MnPSe_3$ and graphite can efficiently reduce the ion migration energy barrier, thereby improving the K^+ storage performance. Therefore, $MnPSe_3$/graphite hybrid can be recognized as general anodes for alkali metal-ion batteries.

2. Experimental section

2.1. Chemicals

Manganese powder (99.3%) was purchased from Alfa Aesar. Red phosphorous powder (97%), selenium powder (99.99%), potassium hexacyanoferrate (II) trihydrate ($K_4Fe(CN)_6{\cdot}3H_2O$, 99.5%), ascorbic acid (>99%), glycol (98%), sodium carboxymethyl cellulose (NaCMC, average Mw ~ 700,000), ethyl carbonate (EC, 99%), dimethyl carbonate (DMC, anhydrous 99.5%), and potassium metal (chunks in mineral oil, 98%) were purchased from Sigma-Aldrich. Potassium chloride (KCl, 99%) was purchased from PubChem. Potassium bis (fluorosulfonyl)imide (KFSI, 97%) was purchased from Combi-Blocks. Lithium hexafluorophosphate ($LiPF_6$), fluoroethylene carbonate (FEC), graphite, super-P, lithium foil, and coin-type cell CR2032 were purchased from shining energy. Glass fiber was purchased from Advantec. Copper was purchased from Chang-Chun group.

2.2. Preparation of bulk $MnPSe_3$

Bulk $MnPSe_3$ was synthesized by a vacuum solid-state method. The manganese powder, red phosphorous powder and selenium powder (the molar ratio is 1:1:3) were heated in the vacuum-sealed quartz tube at 650 °C for 24 h to obtain bulk $MnPS_3$. After completion of the reaction and natural cooling to room temperature, the quartz tube was broken using a diamond cutter and samples were collected.

2.3. Preparation of few layer $MnPSe_3$ and $MnPSe_3$/graphite composites

Few layer $MnPSe_3$ and $MnPSe_3$/graphite composites were synthesized via high-energy mechanical milling (HEMM). Few layer $MnPSe_3$ was prepared by mixing 90 mg of bulk $MnPSe_3$ and 1 mL

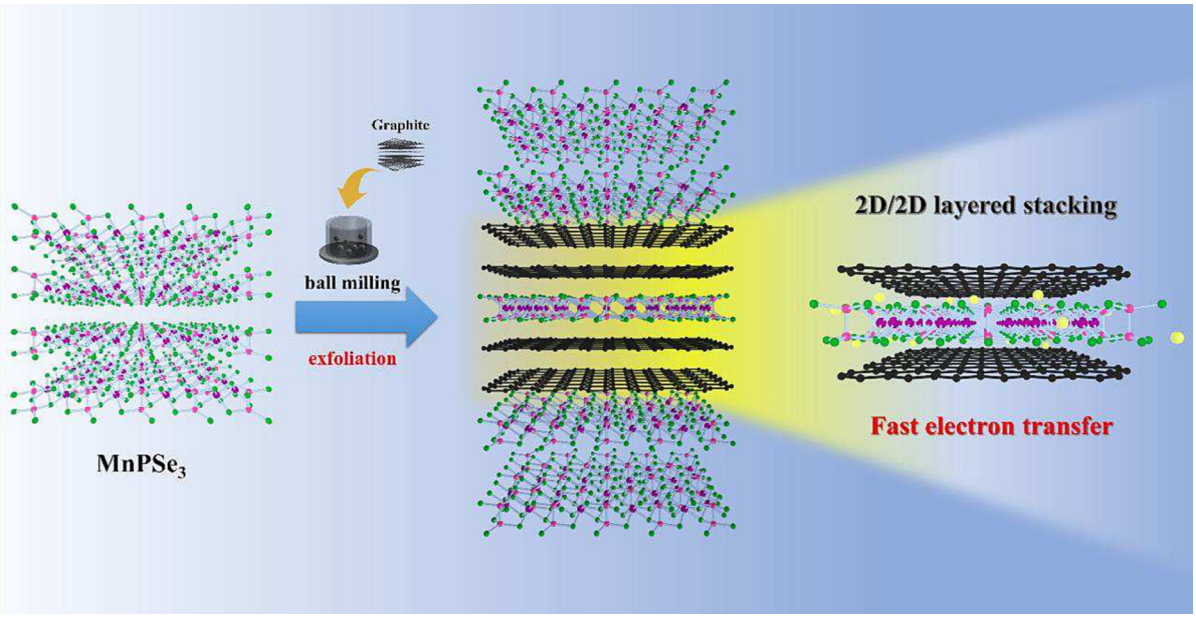

Scheme 1. Schematic illustration of the 2D/2D layered stacking structure with $MnPSe_3$ layers hierarchically stacked in graphite through a high energy ball milling method.

of 2-propanol. The mixture was placed into a stainless-steel jar (12 cm^3) with stainless-steel balls (diameter of 3/8 in.) in a planetary ball mill (PM 100, RETSCH) at a rotation speed of 250 rpm for 24 h. $MnPSe_3$/graphite composites were prepared by mixing 60 mg of bulk $MnPSe_3$ and 30 mg of graphite, which were placed into a stainless-steel jar with stainless-steel balls and sealed inside an argon-filled glovebox. The mass ratio of ball to powder is about 180:1. Finally, the mixture was ball milled for 24 h.

2.4. Synthesis of Prussian blue (PB)

1 g of $FeCl_2{\cdot}4H_2O$ was dissolved in 50 mL of deionized water as solution A. 2.1 g of $K_4Fe(CN)_6{\cdot}3H_2O$, 3.06 g of potassium citrate, 15 g of KCl and 0.5 g of ascorbic acid were dissolved in 100 mL of deionized water as solution B. Solution A was slowly added into solution B under Ar atmosphere and kept at 60 °C for 6 h. The dark blue solid product was centrifuged and washed three times with DI water, and finally dried at 100 °C in a vacuum furnace for 12 h.

2.5. Materials characterization

The crystal purity was determined by X-ray diffractometer (XRD, Bruker D8 ADVANCE) with a Cu-Kα source (λ = 1.54 Å). AFM study was performed by BRUKER Dimension Icon. The morphologies of the obtained samples were examined by employing scanning electron microscopy (SEM, HITACHI-SU8010) and an energy dispersive spectrometer (EDS) was used for elemental mapping. Transmission electron microscopy (TEM, JEOL, JEM-ARM200FTH, serviced provided by NTHU and NCTU) with an accelerating voltage of 200 kV for investigating structural analysis including morphology, crystal d-spacing, and selected-area electron diffraction (SAED). The chemical state was examined by high-resolution X-ray photoelectron spectroscopy (XPS, ULVAC-PH, PHI QuanteraII). All the spectra obtained from XPS analysis were first calibrated by referencing the standard binding energy of C 1s (284.8 eV). Raman spectrum was measured via a LABRAM HR 800 UV with a 532 nm excitation source. TGA analysis was obtained using a thermogravimetric analyzer (TA, Q50) in an air flow at a heating rate of 10 °C min^{-1} from ambient temperature to 800 °C.

2.6. Electrochemical measurements

The homogeneous slurry was prepared by mixing active material (bulk $MnPSe_3$, few layer $MnPSe_3$, $MnPSe_3$/graphite), Super-P, and NaCMC binder with a weight ratio of 7:2:1 onto a copper foil, and then dried under vacuum at 80 °C for 1 h. The average mass loading of the active material is ~ 1 mg·cm^{-2}. For electrochemical test, the half cells were assembled with the potassium foil as the counter electrode, a solution of 1 M potassium bis(fluorosulfonyl) imide (KFSI) in dimethyl carbonate as electrolyte, and glass fiber filters as a separator for PIBs. CR2032 coin cells were assembled in an argon-filled glove box. For LIBs, the half cells were assembled with the lithium foil as the counter electrode, and used 1 M $LiPF_6$ dissolved in ethyl carbonate/dimethyl carbonate (EC: DMC (1:1 vol%)), with 10 wt% additional fluoroethylene carbonate (FEC) as the electrolyte solution. Galvanostatic charge/discharge tests were conducted on Neware battery analyzer (Neware, China) in the potential range of 0.01–3 V (vs. K^+/K). Galvanostatic intermittent titration technique (GITT) was evaluated by Maccor Series 4000 battery test system. Cyclic voltammetry (CV) and electrochemical impedance spectroscopy (EIS) tests were performed on a Biologic VMP3 electrochemistry workstation. For PIB, PB was used as the cathode. For the fabrication of PB electrode, 70 wt% of PB, 10 wt% CNT and 10 wt% NaCMC were mixed with DI water, and the slurry was coated on Al foil, followed by a drying process under vacuum at about 80 °C. To prepare the PIB full cell the mass ratio of cathode/anode is around 3.5:1.

3. Results and discussion

The structure and morphology of the bulk $MnPSe_3$ and $MnPSe_3$/graphite are examined by scanning electron microscopy (SEM) and transmission electron microscopy (TEM). Fig. S1 and Fig. 1a clearly show the typical stacked layered structure of the as-synthesized bulk $MnPSe_3$. The high-resolution transmission electron microscopy (HRTEM) image of $MnPSe_3$ in Fig. 1b confirms that the lattice spacing of 0.184 nm corresponds to the (300) plane of $MnPSe_3$. Furthermore, the selected area electron diffraction (SAED) pattern confirms the single-crystal structure of $MnPSe_3$ (Fig. 1c). After the bulk $MnPSe_3$ and graphite were uniformly

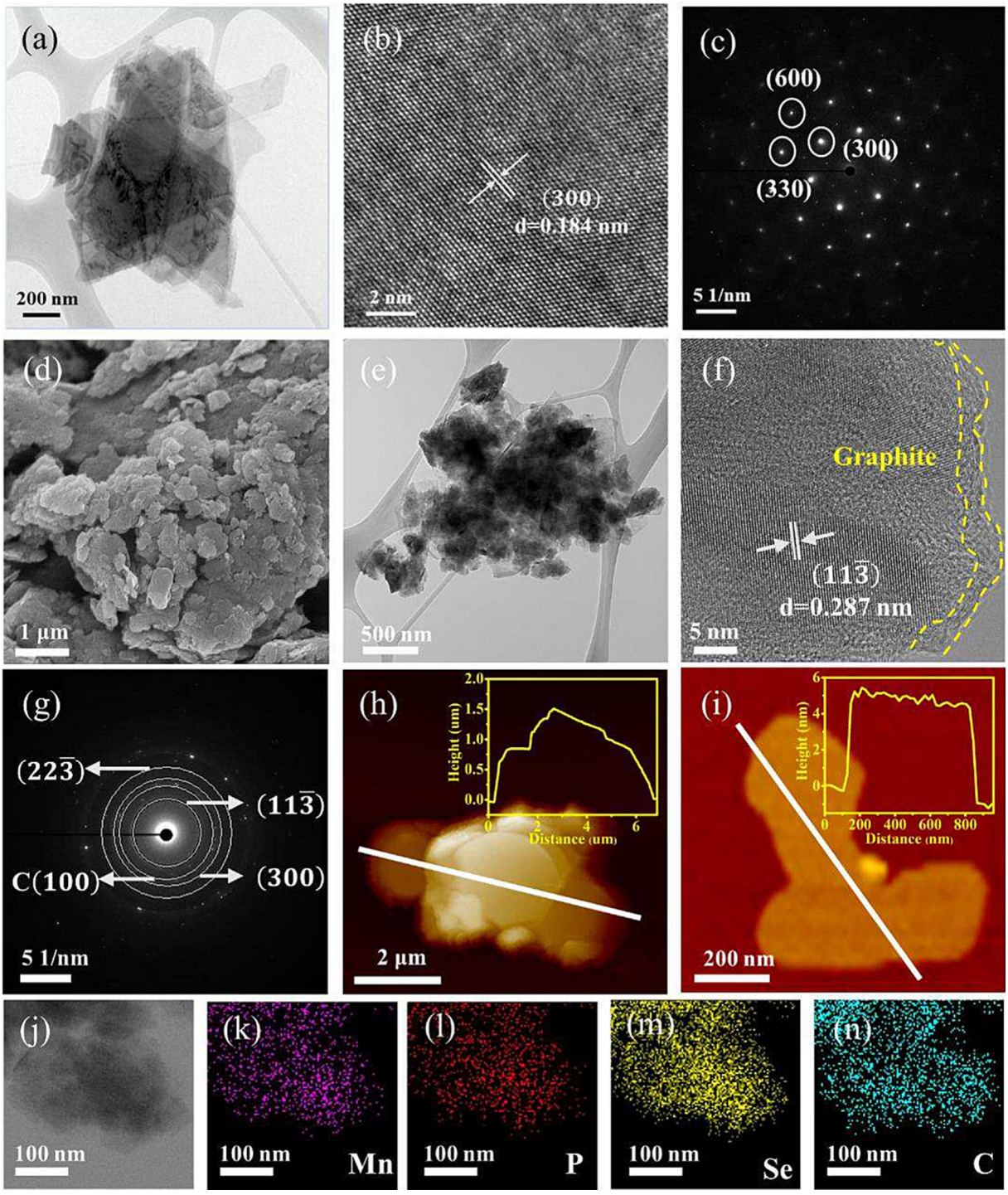

Fig. 1. (a) TEM image, (b) HRTEM image, and (c) SAED image of bulk $MnPSe_3$. (d) SEM image, (e) TEM image, (f) HRTEM image, and (g) SAED image of $MnPSe_3$/graphite. (h and i) AFM image of bulk $MnPSe_3$ and $MnPSe_3$/graphite. (j) STEM image and corresponding (k) Mn, (l) P, (m) Se, and (n) C elemental mapping images of $MnPSe_3$/graphite.

mixed, Fig. 1d and e show an obvious layered structure. The TEM image of $MnPSe_3$/graphite shows that graphite was uniformly dispersed in the $MnPSe_3$ nanosheets after high-efficiency high-energy mechanical milling (HEMM). The HRTEM image of $MnPSe_3$/-graphite in Fig. 1f confirms that the lattice spacing of 0.286 nm corresponds to the (1 1 $\bar{3}$) plane of $MnPSe_3$. On the outermost side of $MnPSe_3$/graphite, a carbon layer is observed, demonstrating that $MnPSe_3$ is successfully distributed in the graphite. The SAED pattern of $MnPSe_3$/graphite in Fig. 1g demonstrates the polycrystalline structure after ball milling. The four diffraction rings can be attributed to the (1 1 $\bar{3}$), (300) and (2 2 $\bar{3}$) planes of $MnPSe_3$ and the (100) plane of graphite, respectively. The thickness of the bulk $MnPSe_3$ and layered $MnPSe_3$ is about 1 μm and 5 nm, respectively, as measured by the height profile by AFM (Fig. 1h and i). The elemental composition measured by scanning TEM energy dispersive spectroscopy (STEM-EDS) element mapping analysis of $MnPSe_3$/-graphite illustrates uniform distribution of manganese (Mn), phosphorous (P), selenium (Se), and carbon (C), as shown in Fig. 1j–n.

The EDS-mapping images of the bulk $MnPSe_3$ demonstrate that Mn, P, and Se elements are homogeneously distributed (Fig. S2). The crystalline structure and phase purity of the as-prepared bulk $MnPSe_3$, few-layer $MnPSe_3$ and $MnPSe_3$/graphite are determined by X-ray diffraction (XRD). As shown in Fig. 2a, all of the diffraction peaks of the three samples are well indexed to the $MnPSe_3$ phase (PDF no. 00–003-0902), and no diffraction peaks from any impurities were detected, indicating the successful synthesis of the three samples. The D-band (1350 cm^{-1}) and G-band (1580 cm^{-1}) in the Raman spectra further confirmed the existence of carbonaceous component in the $MnPSe_3$/graphite [40,41]. The D-band and G-band can reflect the disordered carbon and graphitic carbon [42]. As shown in Fig. 2b, the intensity ratio (I_D/I_G) of $MnPSe_3$/graphite is 1.23. Due to the disordered structure, the K-ion adsorption and insertion capability can be enhanced to further improve the performance. The TGA curve of the $MnPSe_3$/graphite shows that the carbon content can be calculated as about 30% (Fig. S3). The electronic state and surface chemical composition of the bulk $MnPSe_3$ and $MnPSe_3$/graphite were characterized by X-ray photoelectron spectroscopy (XPS) (Figs. 2c–f, S4 and S5). Fig. S4 shows that the presence of the main elements (carbon, manganese, phosphorous, and selenium) for $MnPSe_3$/graphite is confirmed. The C 1s spectrum in Fig. 2c can be deconvoluted into two peaks, where the positions corresponding to 284.8 eV and 285.7 eV are C—C and C—O, respectively [43]. The two peaks at 641.8 and 653.2 eV can be assigned to the Mn(II) $2p_{3/2}$ and Mn(II) $2p_{1/2}$, while the two peaks at 643.4 and 654.8 eV can be attributed to Mn(III) $2p_{3/2}$ and Mn(III) $2p_{1/2}$ (Fig. 2d). As shown in Fig. 2e, a couple of peaks at 132.3 eV and 134 eV are assigned to P $2p_{3/2}$ and P $2p_{1/2}$, respectively. Additionally, the peak at 135.7 eV is attributed to POx due to the surface oxidation of the samples. The Se 3d spectrum in Fig. 2f can be deconvoluted into two peaks with the binding energies of 55 and 56 eV, assigned to Se $3d_{5/2}$ and Se $3d_{3/2}$, respectively [44].

The $MnPSe_3$/graphite electrode was carried out for lithium storage to evaluate the electrochemical performance. Fig. 3a shows the first five CV curves of $MnPSe_3$/graphite under 0.1 mV s^{-1} in the voltage range of 0.01–3.00 V. In the first cycle, the cathodic peak at about 1.72 V, which is ascribed to the formation of solid electrolyte interface (SEI) films. Subsequently, another two peaks appear, which can be attributed to the insertion of Li^+ into $MnPSe_3$ to form Mn, Li_3P, and Li_2Se. During the subsequent anodic process, the anodic peaks can be attributed to the delithiation of Mn, Li_3P, and Li_2Se to form MnSe, Se and amorphous P. All peaks almost overlap after the initial cycle, indicating highly reversible electrochemical performance. Fig. 3b shows the galvanostatic charge/discharge (GCD) curves of $MnPSe_3$/graphite at 0.1 A g^{-1} for 5 cycles. The initial discharge/charge capacity is 684.9/501.5 mA h g^{-1} with a Coulombic efficiency of 73.2%. During the initial discharge–charge process, the irreversible capacity could be caused by the formation of the SEI film and the irreversible reaction [45]. The rate performances of $MnPSe_3$, few-layer $MnPSe_3$ and $MnPSe_3$/graphite electrodes were obtained as shown in Fig. 3c. It can be observed that the rate performances of bulk $MnPSe_3$ and few-layer $MnPSe_3$ electrodes were dissatisfaction. Conversely, the $MnPSe_3$/graphite electrode delivers a specific capacity of 621.7, 496.1, 432.5, 376, 316.6, 275, 237.8 and 194.4 mA h g^{-1} at a current density of 0.1, 0.5, 1, 2, 4, 6, 8, and 10 A g^{-1}, respectively. The results show that the rate performance of $MnPSe_3$/graphite electrode is higher than that of the bulk $MnPSe_3$ and few-layer $MnPSe_3$ electrodes. Figs. 3d, e and S5 show the cyclic performances of bulk $MnPSe_3$, few-layer $MnPSe_3$ and $MnPSe_3$/graphite at the current density of 0.1, 2 and 3 to 5 A g^{-1}, respectively. The discharge capacities of the $MnPSe_3$/graphite electrode are 912.9 mA h g^{-1} at 0.1 A g^{-1} after 100 cycles, and 488.1 mA h g^{-1} at 2 A g^{-1} after 500 cycles. Even to 4 A g^{-1}, the of the $MnPSe_3$/graphite electrode delivers the discharge capacity of 405.6 mA h g^{-1} after 500 cycles. Obviously, the cycling performance of the $MnPSe_3$/graphite electrode is better than that of the bulk $MnPSe_3$ and few-layer $MnPSe_3$ electrodes.

Inspired by the excellent performance of $MnPSe_3$/graphite in LIB, we also investigated the PIB system using the $MnPSe_3$/graphite anode. Fig. 3f shows the CV curves of the $MnPSe_3$/graphite electrode for PIB at a scan rate of 0.1 mV s^{-1}. This result is different from that in Fig. 3a. The two cathodic peaks are at about 1.15 V and 0.95 V during the first cycle, corresponding to the formation

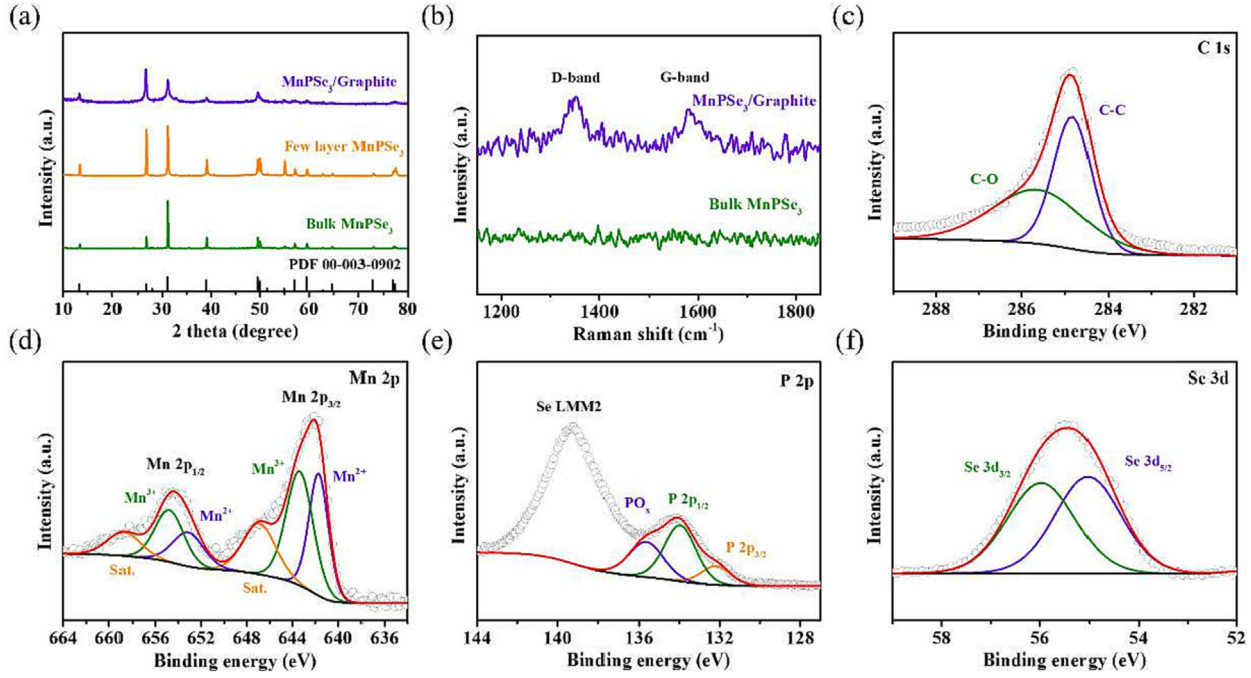

Fig. 2. (a) XRD patterns of bulk $MnPSe_3$, few layer $MnPSe_3$, and $MnPSe_3$/graphite. (b) Raman spectra of bulk $MnPSe_3$ and $MnPSe_3$/graphite. (c–f) High-resolution C 1s, Mn 2p, P 2p, and Se 3d XPS spectra of $MnPSe_3$/graphite.

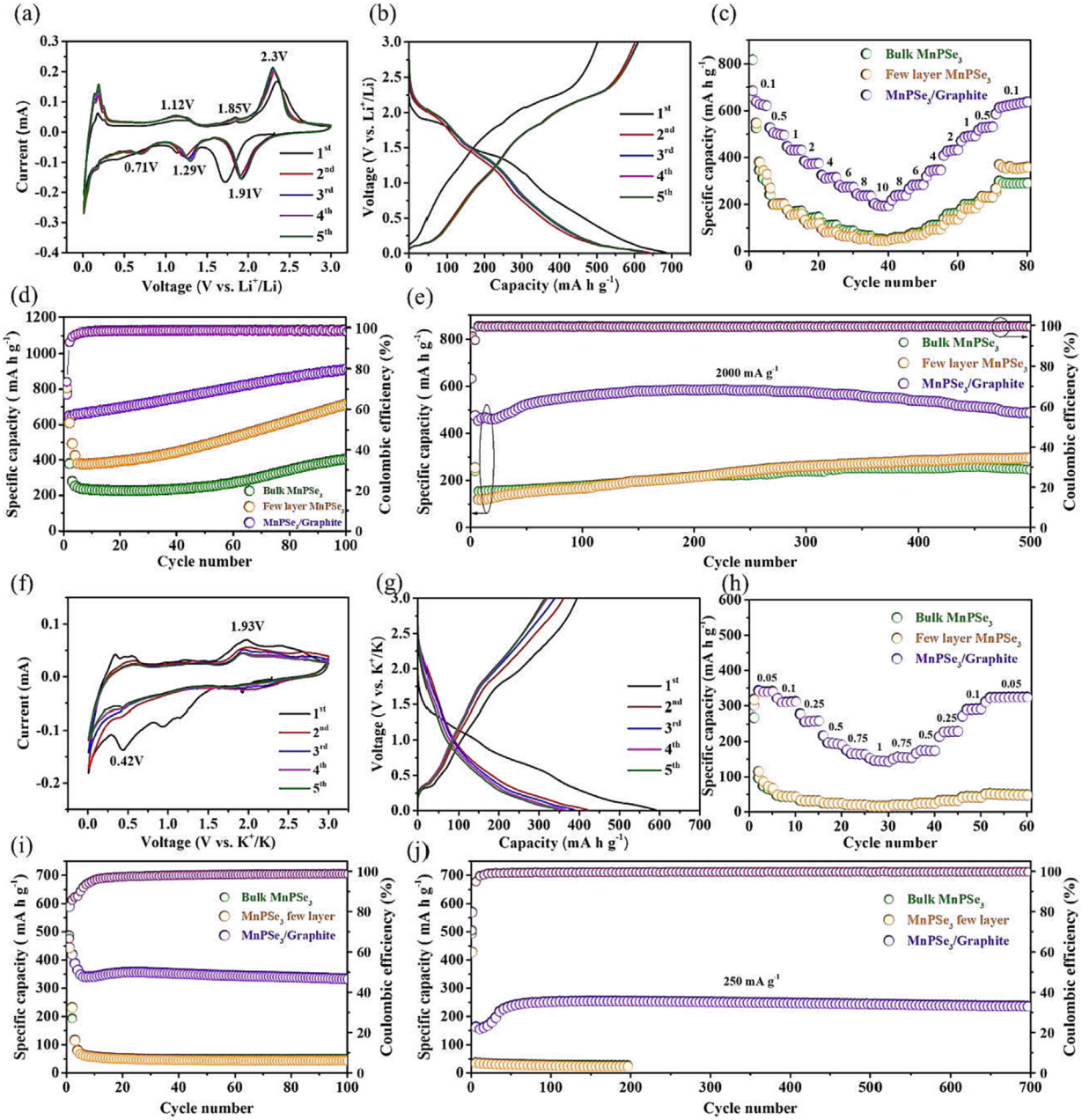

Fig. 3. (a) CV profiles at a scan rate of 0.1 mV s^{-1} and (b) GCD curves at 100 mA g^{-1} of $MnPSe_3$/graphite in LIB. (c) Rate performance at various current densities from 0.05 to 10 A g^{-1}, and cycling performance at (d)100 mA g^{-1} and (e) 2000 mA g^{-1} of bulk $MnPSe_3$, few layer $MnPSe_3$, and $MnPSe_3$/graphite in LIB. (f) CV profiles at a scan rate of 0.1 mV s^{-1} and (g) GCD curves at 50 mA g^{-1} of $MnPSe_3$/graphite in PIB. (h) Rate performance at various current densities from 0.05 to 1 A g^{-1}, and cycling performance at (i) 50 mA g^{-1} and (j) 250 mA g^{-1} of bulk $MnPSe_3$, few layer $MnPSe_3$, and $MnPSe_3$/graphite in PIB.

of the SEI film and the irreversible reaction, respectively. Another cathodic peak at 0.5 V can be attributed to the formation of Mn, K_4P_3 and K_2Se. During the anodic process, the peak of 1.96 V originates from the depotassiation of Mn, K_4P_3 and K_2Se to form $MnPSe_3$. As shown in Fig. 3g, the $MnPSe_3$/graphite electrode delivers the first charge/discharge capacities of 589.9/394.1 mA h g^{-1} with an initial Coulombic efficiency of 66.8%. The rate performance and cycling performance of the bulk $MnPSe_3$, few-layer $MnPSe_3$, and $MnPSe_3$/graphite are compared for PIBs. Fig. 3h shows the discharge capacities of the $MnPSe_3$/graphite electrode are 341.1, 312.5, 258.8, 190.9, 163.6 and 143.3 mA h g^{-1} at current densities of 0.05, 0.1, 0.25, 0.75 and 1 A g^{-1}, respectively.

The $MnPSe_3$/graphite electrode delivers 334 mA h g^{-1} at current densities of 0.05 A g^{-1} for 100 cycles and 236.7 mA h g^{-1} at current densities of 0.25 A g^{-1} for 700 cycles (Fig. 3i and j), indicating that it has an excellent performance in PIB. The cycle performance of the $MnPSe_3$/graphite electrode at higher current densities is shown in Fig. S7, observing that the $MnPSe_3$/graphite electrode delivers 268.4 mA h g^{-1} at 0.3 A g^{-1} for 100 cycles. Additionally, the cycle performance of MnPSe3 with different carbon ratios ($MnPSe_3$: graphite = 3:1, 4:1, 5:1) are investigated (Fig. S8). In contrast, the capacity of bulk $MnPSe_3$ and few-layer $MnPSe_3$ decay rapidly. Compared with the bulk $MnPSe_3$ and few-layer $MnPSe_3$, the graphite as a protective layer in the $MnPSe_3$/graphite can relieve the contact stress between $MnPSe_3$ nanosheets and reduce the damage to the electrode structure during the electrochemical process, thereby significantly improving the cycling stability. The introduc-

tion of graphite can not only improve the electron conductivity, but also mitigate the volume expansion of the electrode.

To investigate the electrochemical kinetics of the $MnPSe_3$/-graphite, the capacitive contribution of the LIB and PIB system was first performed, and CV profiles were examined at various scan rates from 0.1 to 1 mV s^{-1} (Fig. 4). The CV curves of $MnPSe_3$/-graphite show similar shapes at different scanning rates for the Li and K storage. The relationship between the peak current (i) and the scan rate (v) is described by equation i = avb, which can be used to confirm whether the reaction is a slow diffusion process or a fast surface-controlled process [46,47]. In general, the b-value approaches 0.5 for a typical diffusion-controlled process, and 1.0 for a surface capacitive-controlled process [48,49]. Interestingly, as presented in Fig. 4b and f, the b values of the $MnPSe_3$/graphite electrode approach to 1.0 for LIB and 0.6 for PIB, indicating the electrochemical processes for LIB and PIB are dominated by surface-mediated capacitive behavior and the co-existence of both capacitive behavior and diffusion behavior, respectively. Furthermore, capacitive and diffusion-controlled storage contributions are quantified according to the following equation: $i = k_1v + k_2v^{1/2}$ (k_1: capacitive behavior, k_2: ionic diffusion behavior) [50,51]. As shown in Fig. 4b and f, the $MnPSe_3$/graphite electrode at 0.6 mV s^{-1} presents 89% and 31% of the pseudocapacitance contribution for LIB and PIB, respectively. Although both of the contribution of capacitance gradually increases when the scan rate increases (Fig. 4d and h), the values are low in PIB, indicating that the $MnPSe_3$/graphite electrode has fast reaction kinetics in LIB, resulting in excellent rate performance. The kinetic mechanism of LIB is quite different from that of PIB, which is due to the slow kinetics caused by the excessively large radius of potassium ions. Moreover, the diffusion coefficient of Li^+/K^+ in the $MnPSe_3$/graphite electrode is evaluated by the galvanostatic intermittent titration technique (GITT) based on the equation as follows: $D_{K^+} = \frac{4}{\pi\tau}\left(\frac{m_B V_M}{M_B S}\right)^2\left(\frac{\Delta E_S}{\Delta E_\tau}\right)^2$ ($\tau \ll \frac{L^2}{D}$), where τ is the relaxation time; m_B, M_B and V_M are the mass, molar mass and molar volume of the electrode material; S is the electrode–electrolyte interfacial area; ΔEs is the voltage change caused by the pulse current; ΔEt is voltage change during the constant current pulse [52,53]. Furthermore, GITT curves of the $MnPSe_3$/graphite electrode can be obtained during the discharge/charge process under 0.05 A g^{-1} for 20 mins with rest intervals of 1 h (Fig. 4i and k). Notably, during the charge and discharge process, the average diffusion coefficients for Li^+ and K^+ are 1.07 × 10^{-10} cm^2 s^{-1} and 6.13 × 10^{-11} cm^2 s^{-1} (Fig. 4j and l). This result indicates that the $MnPSe_3$/graphite electrode exhibits rapid Li^+/K^+ diffusion due to the introduction of graphite. In addition, in-situ electrochemical impedance spectroscopy (EIS) was performed (Fig. S9). The results show that the $MnPSe_3$/graphite exhibits excellent electrochemical kinetics.

In order to study the phase transition of $MnPSe_3$ during the lithiation/delithiation process, *in–situ* XRD and *ex–situ* TEM were performed. Fig. 5a presents the *in-situ* XRD pattern of $MnPSe_3$ for the initial cycles along with the corresponding charge/discharge curves. After the insertion of Li^+, the intensity of the diffraction peaks of $MnPSe_3$ gradually decreased. When discharged to 0.01 V, several peaks are observed at 25.6°, 29.6°, 42.5°, and 42.9°, corresponding to the Li_2Se (PDF no. 04–003-6918), Li_3P (PDF no. 04–014-7866) and Mn (PDF no. 00–033-0887). Then, the peaks of Li_2Se, Li_3P and Mn gradually disappear when charging from 0.01 V to 3 V, and there are three strong peaks at 25.7°, 29.8°, and 42.6°, which are attributed to Se (PDF no. 00–051-1389) and MnSe (PDF no. 01–073-1742), indicating that the reaction is irreversible in the first cycle. As shown in Fig. 5b, the *ex-situ* HRTEM image of the $MnPSe_3$/graphite electrode after discharge

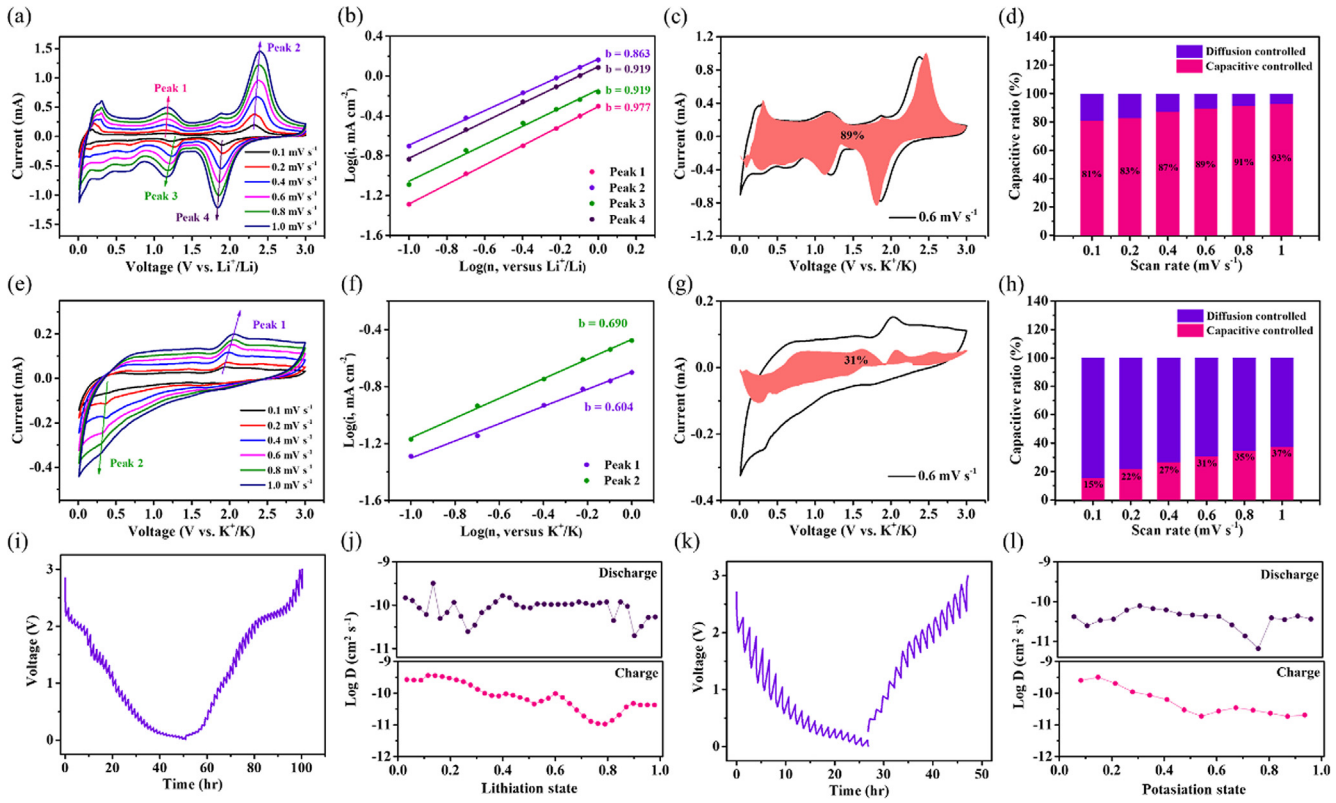

Fig. 4. CV curves at various scan rates in the range of 0.1–1.0 mV s^{-1}, log(*i*) *versus* log(*v*) plots at specific peak currents, capacitive contribution at the scan rate of 0.6 mV s^{-1}, and contribution ratio of the capacitive and diffusion-controlled capacities for $MnPSe_3$/graphite in LIBs (a–d) and PIBs (e–h). GITT analysis of MnPSe3/graphite at 0.05 A g^{-1} and the calculated ion diffusion coefficient in LIBs (i and j) and PIBs (k and l).

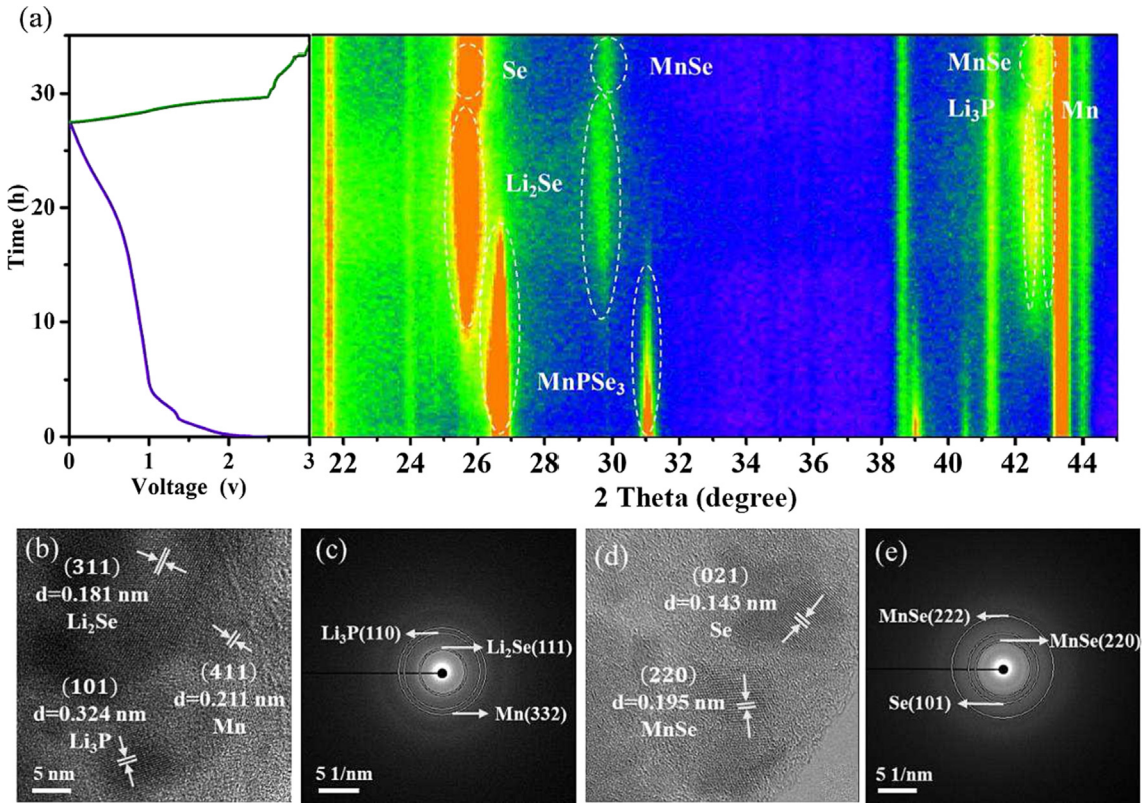

Fig. 5. (a) In-situ XRD pattern of $MnPSe_3$ during the first lithiation/delithiation process. HRTEM and SAED images of $MnPSe_3$ after (b and c) discharging to 0.01 V and (d and e) charging to 3.0 V.

to 0.01 V show three characteristic lattices spacing of 0.211, 0.324 and 0.181 nm, indexed to (411), (101) and (311) of Mn, Li_3P and Li_2Se, respectively. The corresponding diffraction spots of the SAED test also confirmed the existence of Mn, Li_3P and Li_2Se in Fig. 5c. At the fully charged state (0.03 V), ex situ HRTEM and SAED images of the $MnPSe_3$/graphite electrode prove the irreversible reaction (Fig. 5d and e). Because the P element cannot be observed from both *in-situ* XRD, HRTEM and SAED, it is speculated that amorphous P is formed after delithiation. Based on the above results, the conversion mechanism of $MnPSe_3$/graphite for LIB can be summarized as: $MnPSe_3 + 9Li^+ + 9e^- \rightarrow Li_3P + 3Li_2Se + Mn$ for the discharge process, and $Li_3P + 3Li_2Se + Mn \rightarrow MnSe + 2Se + P$ (amorphous) $+ 9Li^+ + 9e^-$ for the charge process.

Based on the CV curve and GCD curve of the $MnPSe_3$/Graphite electrode for LIB and PIB, it can be found that the reaction for Li storage is different from that for K storage. Therefore, *ex-situ* XRD and *ex-situ* TEM were performed to understand the K^+-storage mechanism (Fig. 6). When discharging from OCV to 0.01 V, the new peaks were observed at 28.5°, 29.7°, 33.2°, and 42.7°, assigned to K_4P_3 (PDF no. 04–007-1643), K_2Se (PDF no. 04–003-6925), and Mn, respectively. When fully charged to 3.0 V, the diffraction peaks of K_2Se, K_4P_3, and Mn completely disappear while the peaks of $MnPSe_3$ reappear, indicating that it is a reversible reaction and a different form from that in LIB. In addition, *ex-situ* TEM was used to investigate the morphological and phase evolutions of $MnPSe_3$/-graphite at a fully discharged state (0.01 V) and fully charged state (3.0 V). When discharged to 0.01 V, some lattice fringes with lattice spacings with 0.207, 0.310, and 0.233 nm can be clearly observed, corresponding to the (411), (024), and (311) planes of Mn, K_4P_3, and K_2Se, respectively (Fig. 6c). The corresponding SAED in Fig. 6d shows that the d-spacing of the diffraction rings can be assigned to the Mn (332) plane, K_2Se (220) plane and K_4P_3 (113) plane. When charged to 3 V, the lattice fringes of $MnPSe_3$ were detected in Fig. 6f, and the d-spacing of the diffraction rings can be assigned to $MnPSe_3$ in Fig. 6g. This is in good agreement with the results of ex situ XRD (Fig. 6a). As a result, the reversible conversion mechanism of $MnPSe_3$/graphite for PIB can be summarized as: $3MnPSe_3 + 22\ K^+ + 22e^- \leftrightarrow 3K_4P_3 + 9K_2Se + 3Mn$, thereby allowing 22 electrons to transfer. The EDS-mapping images demonstrate that K, Mn, P, and Se elements are homogeneously distributed (Fig. 6h–l).

In order to gain insight into the reasons for the enhanced K^+ storage performance, density functional theory (DFT) calculations are performed to further investigate the effect of the carbon layer on the performance of the $MnPSe_3$-based anode. To reveal the electronic properties of $MnPSe_3$/graphite, Fig. 7a and b show the electronic band structures of bulk $MnPSe_3$ and $MnPSe_3$/graphite. It can be observed that the bulk $MnPSe_3$ is a semiconductor material with a large band gap of 1.72 eV, indicating the conductivity is relatively poor against the electron transfer. Importantly, Fig. 7b shows that the band gap decreases to 0.07 eV due to the energy band contributed by graphite. In addition, the total density of states (DOS) of bulk $MnPSe_3$ and $MnPSe_3$/graphite was explored (Fig. 7c and d). It can be found that $MnPSe_3$/graphite has a continuous electronic state near the Fermi level is higher than that of bulk $MnPSe_3$, showing that the addition of graphite enhances the conductivity. Furthermore, the difference in charge density shows that the charge state of $MnPSe_3$/graphite is more stable than that of bulk $MnPSe_3$ and few layer $MnPSe_3$ because part of the charge is transferred to the graphite during the potassiation process (Fig. 7e–h). Fig. 7i–k display the side views of K^+ migration paths in bulk $MnPSe_3$, few layer $MnPSe_3$, and $MnPSe_3$/graphite, corresponding to the potassium diffusion pathways between $MnPSe_3$ layers, on the surface of $MnPSe_3$ layer, and between $MnPSe_3$ and graphite, respectively. The corresponding migration energy barriers of bulk $MnPSe_3$, few layer $MnPSe_3$, and $MnPSe_3$/graphite were shown in

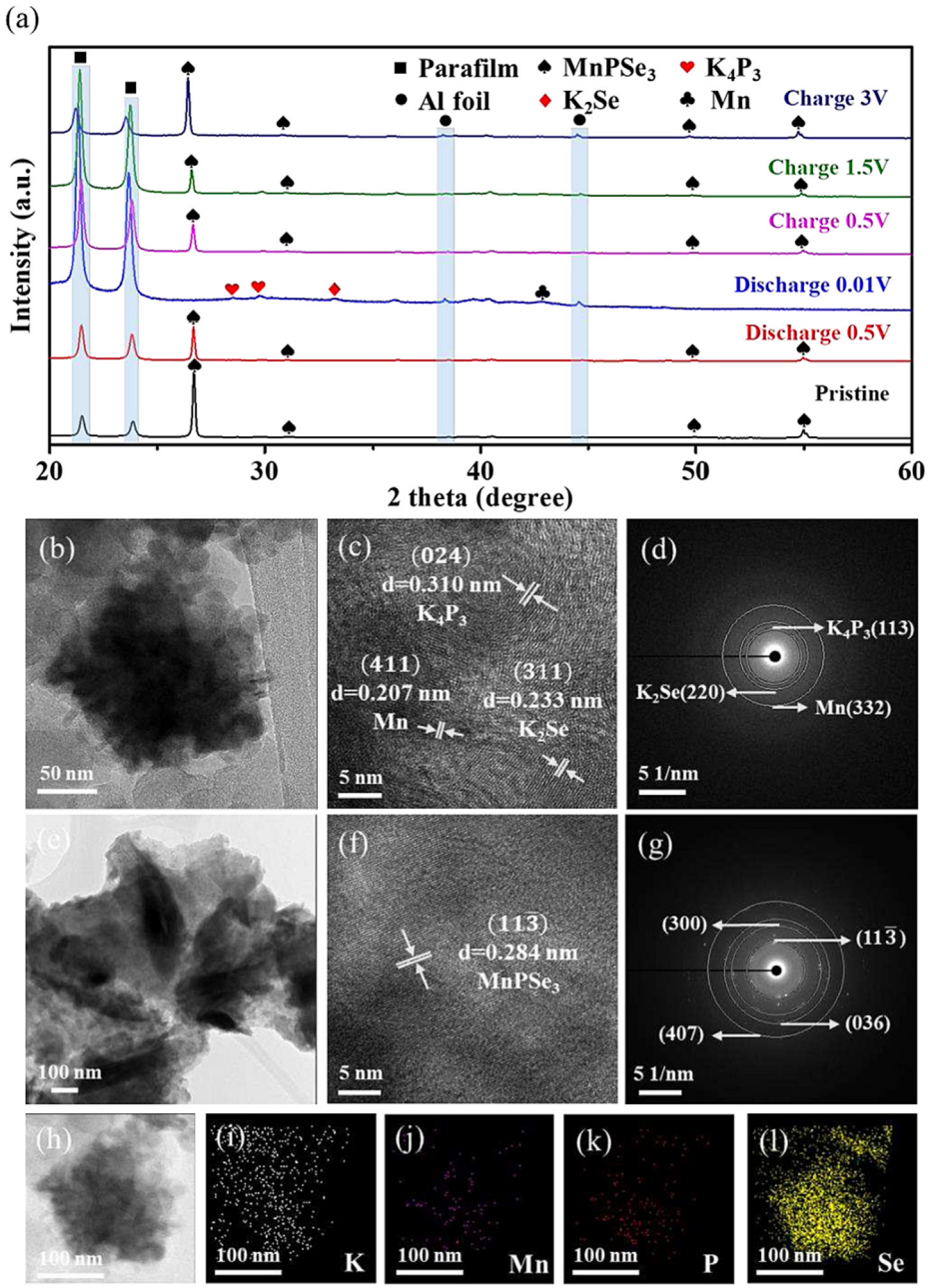

Fig. 6. (a) *Ex-situ* XRD patterns of $MnPSe_3$ during the first potassiation/depotassiation process. TEM, HRTEM and SAED images of the $MnPSe_3$ electrode after (b-d) discharging to 0.01 V and (e-g) charging to 3.0 V. (h–l) EDS mapping images of $MnPSe_3$ after discharging to 0.01 V.

Fig. 7l. It can be observed that the calculated diffusion energy barriers of few layer $MnPSe_3$ and $MnPSe_3$/graphite are lower than that of bulk $MnPSe_3$, indicating their K^+ requires only lower energy to diffuse through. Although the calculated diffusion energy barriers of few layer $MnPSe_3$ are low, the electrochemical performance is still poor after exfoliated, which may be attributed to the nanosheet agglomeration during the charge and discharge process. These results suggest that this 2D/2D structure formed by the stacked of few-layer $MnPSe_3$ on the graphite can be improved to obtain good performance. Therefore, the construction design of the $MnPSe_3$/graphite composite is favorable for the rapid transfer of electrons to improve the reaction kinetics.

To show the practical performance of $MnPSe_3$/graphite, a full PIB cell with $MnPSe_3$/graphite as anode and Prussian blue (PB) as cathode was assembled (Fig. 8a). Related material characterizations and electrochemical tests of the PB cathode are shown in Figs. S10 and S11. The GCD curves of the $MnPSe_3$/graphite//K half-cell, PB//K half-cell and $MnPSe_3$/graphite//PB full-cell are shown in Fig. 8b. The working voltage of the $MnPSe_3$/graphite//PB full-cell ranges from 1 to 3.8 V, which is between that of $MnPSe_3$/graphite//K and PB//K half-cell. Fig. S12 shows the CV curves of $MnPSe_3$/graphite//PB at a scan rate of 1 mV s^{-1}. The overlapping peaks indicate that the full cell is in the proper voltage window of 1.0–3.8 V. Fig. 8c shows the initial charge and discharge capacity are 46.1 and 44 mA h g^{-1}, and the overlapping shapes indicate good reversibility and stability. Fig. 8d shows the excellent rate performance of the $MnPSe_3$/graphite full cell. As the current density increases from 0.1 A g^{-1} to 1.0 A g^{-1}, the full cell shows the capacities of 49.9, 44.3, 38.7, 34.1, and 30.5 mA h g^{-1}(based on the mass of the cathode), respectively. Notably, the $MnPSe_3$/-

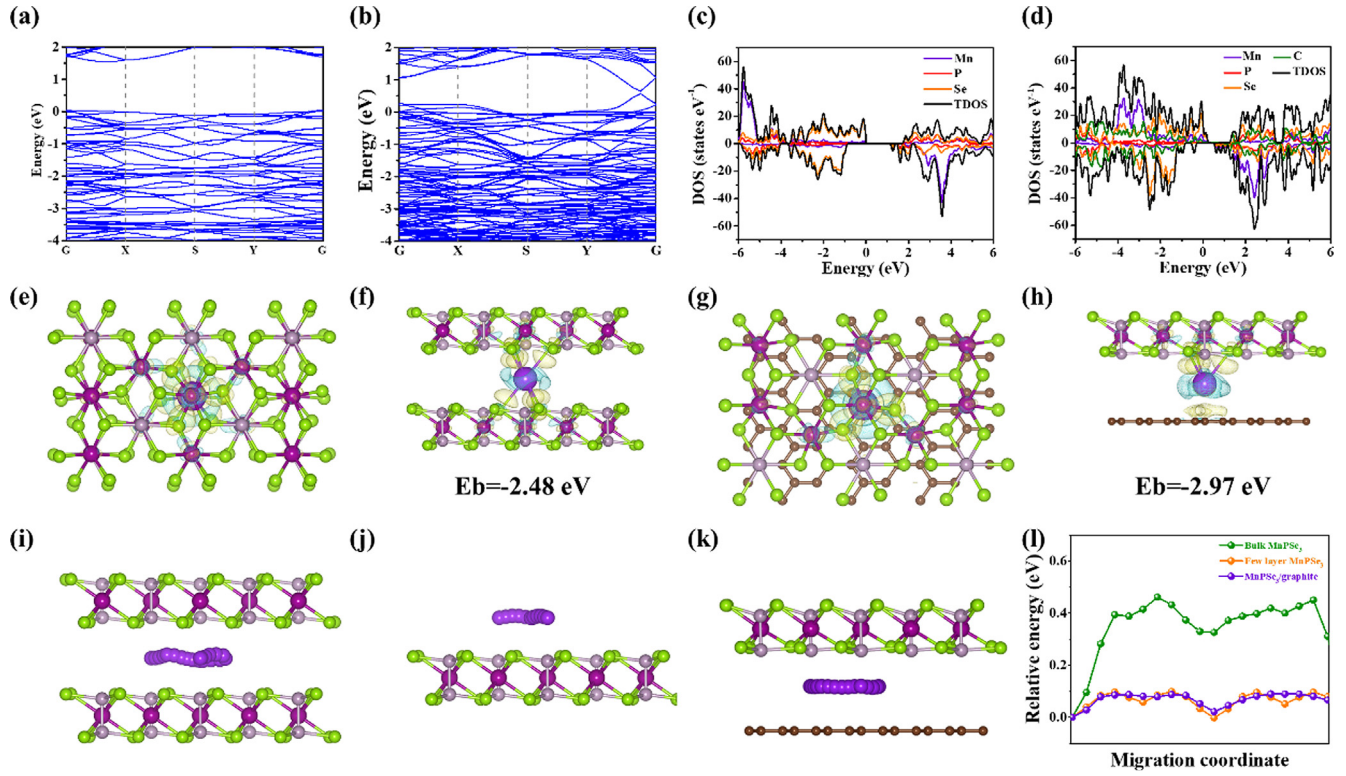

Fig. 7. (a and b) Band structures and (c and d) calculated TDOS of bulk $MnPSe_3$ and $MnPSe_3$/graphite hybrid. Charge density differences of K^+ adsorbed on (e and f) bulk $MnPSe_3$ and (g and h) MnPSe3/graphite for top view and side view. The side of potassium diffusion pathways (i) between $MnPSe_3$ layers, (j) on the surface of $MnPSe_3$ layer, and (k) between $MnPSe_3$ and graphite. (l) Calculated energy barriers of K between $MnPSe_3$ layers, and between $MnPSe_3$ and graphite.

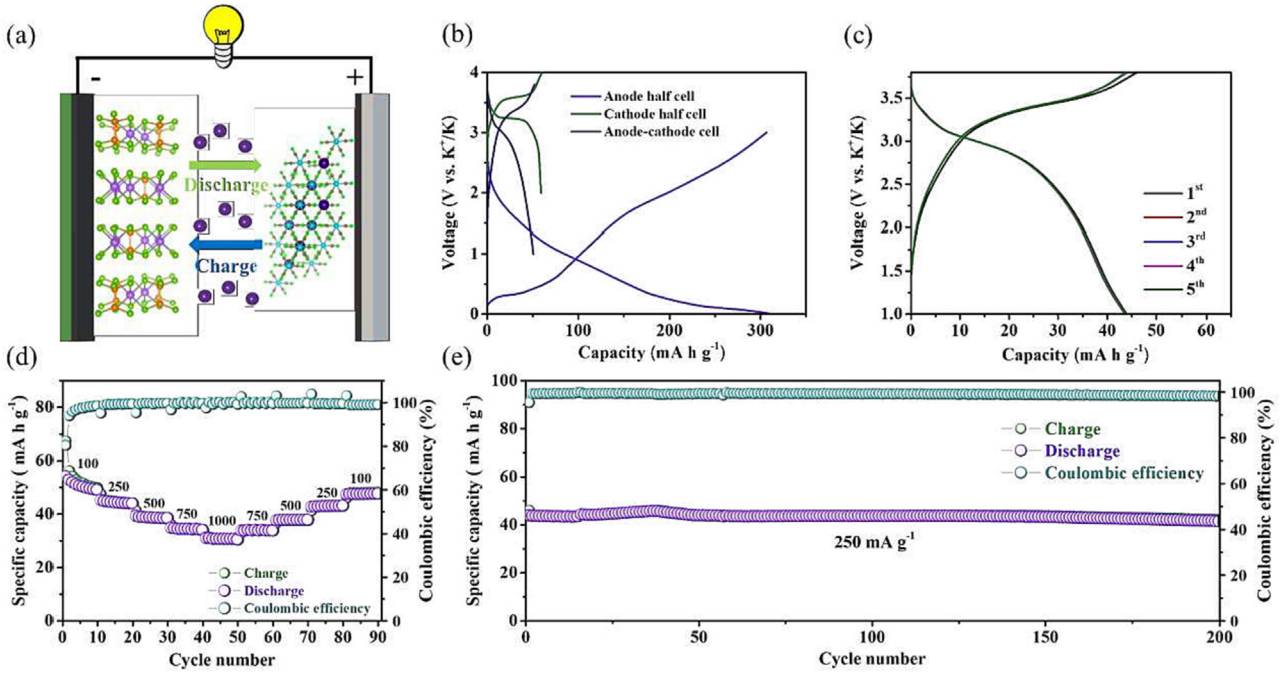

Fig. 8. (a) Schematic diagram of a $MnPSe_3$/graphite//PB full cell. (b) GCD curves of PB//K and $MnPSe_3$/graphite//K half cells and a $MnPSe_3$/graphite//PB full cell. (c) GCD curves at 100 mA g^{-1}. (d) Rate performance at current densities ranging from 0.1 to 1 A g^{-1}. (e) Long-term cycling performance at 250 mA g^{-1}.

graphite full cell delivers the capacities of 42.2 mA h g^{-1} after 200 cycles at 0.25 A g^{-1}, with a high capacity retention rate of 91.5% (Fig. 8e), indicating that $MnPSe_3$/graphite is a promising candidate for practical applications anode.

4. Conclusion

In conclusion, $MnPSe_3$ is used as anode for LIB and PIB due to layered structure, magnetic properties, abundant resources and

low cost of manganese. Notably, 2D/2D $MnPSe_3$/graphite hybrid has been successfully fabricated by ball milling. We reveal this unique 2D/2D structure formed by the stacked of few-layer $MnPSe_3$ on the graphite. Conductive graphite can serve as an effective buffer to avoid nanosheet aggregation and huge volume change. When used as anode for LIB and PIB, the optimized $MnPSe_3$ nanosheets exhibit excellent electrochemical performance. The $MnPSe_3$/graphite electrode exhibits 488.1 mA h/g after 500 cycles at 2000 mA/g in LIB and 236.7 mA h after 700 cycles at 250 mA/g in PIB. Moreover, the reversible conversion mechanism of $MnPSe_3$/graphite for PIB is explored for the first time, and is successfully revealed based on 22 electrons transfer. Furthermore, based on DFT calculations, the performance of $MnPSe_3$/graphite hybrids as anode materials for LIB and PIB are assessed. The band gap of $MnPSe_3$/graphite decreases to 0.07 eV, indicating that the conductivity of $MnPSe_3$ is enhanced by the introduction of graphite. Therefore, the 2D/2D $MnPSe_3$/graphite composite can be expected to draw interest for the anode material in energy storage system.

CRediT authorship contribution statement

Yan-Fu Huang: Conceptualization, Methodology, Data curation. **Yi-Chun Yang:** Methodology, Data curation. **Yen-Yang Tseng:** Data curation. **Hsing-Yu Tuan:** Conceptualization, Resources, Supervision, Writing – review & editing.

Data availability

No data was used for the research described in the article.

Declaration of Competing Interest

The authors declare that they have no known competing financial interests or personal relationships that could have appeared to influence the work reported in this paper.

Acknowledgements

This work was supported by the financial support from the 2030 Cross-Generation Young Scholars Program by Ministry of Science and Technology, Taiwan (111-2628-E-007 -008). H.-Y. Tuan also acknowledges the financial support of National Tsing Hua University, Taiwan, through the grant of 111QI030E1.

Appendix A. Supplementary material

Supplementary data to this article can be found online at https://doi.org/10.1016/j.jcis.2022.12.082.

References

[1] Z. Zhu, Z. Xu, The rational design of biomass-derived carbon materials towards next-generation energy storage: a review, Renew. Sust. Energ. Rev. 134 (2020) 110308.
[2] M. Hannan, S. Wali, P. Ker, M. Abd Rahman, M. Mansor, V. Ramachandaramurthy, K. Muttaqi, T. Mahlia, Z. Dong, Battery energy-storage system: a review of technologies, optimization objectives, constraints, approaches, and outstanding issues, J. Energy Storage 42 (2021) 103023.
[3] H. Wang, C. Zhu, D. Chao, Q. Yan, H.J. Fan, Nonaqueous hybrid lithium-ion and sodium-ion capacitors, Adv. Mater. 29 (2017) 1702093.
[4] W. Liu, P. Oh, X. Liu, M.-J. Lee, W. Cho, S. Chae, Y. Kim, J. Cho, Nickel-rich layered lithium transition-metal oxide for high-energy lithium-ion batteries, Angew. Chem. Int. Ed. 54 (15) (2015) 4440–4457.
[5] Y. Zhang, L. Wang, H. Xu, J. Cao, D. Chen, W. Han, 3D chemical cross-linking structure of black phosphorus@ CNTs hybrid as a promising anode material for lithium ion batteries, Adv. Funct. Mater. 30 (2020) 1909372.
[6] H. Li, W. Zhang, K. Sun, J. Guo, K. Yuan, J. Fu, T. Zhang, X. Zhang, H. Long, Z. Zhang, Manganese-based materials for rechargeable batteries beyond lithium-ion, Adv. Energy Mater. 11 (2021) 2100867.
[7] D. Larcher, J.-M. Tarascon, Towards greener and more sustainable batteries for electrical energy storage, Nature Chem. 7 (1) (2015) 19–29.
[8] X. Zeng, M. Li, D. Abd El-Hady, W. Alshitari, A.S. Al-Bogami, J. Lu, K. Amine, Commercialization of lithium battery technologies for electric vehicles, Adv. Energy Mater. 9 (2019) 1900161.
[9] K. Chayambuka, G. Mulder, D.L. Danilov, P.H.L. Notten, From li-ion batteries toward Na-ion chemistries: challenges and opportunities, Adv. Energy Mater. 10 (38) (2020) 2001310.
[10] R. Verma, P.N. Didwal, J.-Y. Hwang, C.-J. Park, Recent progress in electrolyte development and design strategies for next-generation potassium-ion batteries, Batteries Supercaps 4 (9) (2021) 1428–1450.
[11] M. Chen, Q. Liu, Z. Hu, Y. Zhang, G. Xing, Y. Tang, S.L. Chou, Designing advanced vanadium-based materials to achieve electrochemically active multielectron reactions in sodium/potassium-ion batteries, Adv. Energy Mater. 10 (2020) 2002244.
[12] C. Zhang, H. Zhao, Y. Lei, Recent research progress of anode materials for potassium-ion batteries, Energy Environ. Mater. 3 (2) (2020) 105–120.
[13] H. Dai, Z. Zeng, X. Yang, M. Jiang, Y. Wang, Q. Huang, L. Liu, L. Fu, P. Zhang, Y. Wu, Superior potassium storage behavior of hard carbon facilitated by ether-based electrolyte, Carbon 179 (2021) 60–67.
[14] S. Duehnen, J. Betz, M. Kolek, R. Schmuch, M. Winter, T. Placke, Toward green battery cells: perspective on materials and technologies, Small Methods 4 (2020) 2000039.
[15] C. Zhang, H. Pan, L. Sun, F. Xu, Y. Ouyang, F. Rosei, Progress and perspectives of 2D materials as anodes for potassium-ion batteries, Energy Stor. Mater. 38 (2021) 354–378.
[16] M. Sajjad, F. Cheng, W. Lu, Research progress in transition metal chalcogenide based anodes for K-ion hybrid capacitor applications: a mini-review, RSC Adv. 11 (41) (2021) 25450–25460.
[17] N.a. Li, Y. Li, X. Zhu, C. Huang, J.-J. Kai, J. Fan, Theoretical investigation of the structure–property correlation of mxenes as anode materials for alkali metal ion batteries, J. Phys. Chem. C 124 (28) (2020) 14978–14986.
[18] Y.-S. Xu, S.-Y. Duan, Y.-G. Sun, D.-S. Bin, X.-S. Tao, D. Zhang, Y. Liu, A.-M. Cao, L.-J. Wan, Recent developments in electrode materials for potassium-ion batteries, J. Mater. Chem. A 7 (9) (2019) 4334–4352.
[19] H. Zhang, D. Yang, A. Lau, T. Ma, H. Lin, B. Jia, Hybridized graphene for supercapacitors: beyond the limitation of pure graphene, Small 17 (2021) 2007311.
[20] Q. Liang, Q. Zhang, X. Zhao, M. Liu, A.T. Wee, Defect engineering of two-dimensional transition-metal dichalcogenides: applications, challenges, and opportunities, ACS Nano 15 (2021) 2165–2181.
[21] J. Cheng, L. Gao, T. Li, S. Mei, C. Wang, B. Wen, W. Huang, C. Li, G. Zheng, H. Wang, Two-dimensional black phosphorus nanomaterials: emerging advances in electrochemical energy storage science, Nano-Micro Lett. 12 (2020) 1–34.
[22] H. Liu, K. Sun, X. Shi, H. Yang, H. Dong, Y. Kou, P. Das, Z.-S. Wu, Q. Shi, Two-dimensional materials and their derivatives for high performance phase change materials: emerging trends and challenges, Energy Stor. Mater. 42 (2021) 845–870.
[23] R. Cao, S. Fan, P. Yin, C. Ma, Y. Zeng, H. Wang, K. Khan, S. Wageh, A.A. Al-Ghamd, A.K. Tareen, A.G. Al-Sehemi, Z. Shi, J. Xiao, H. Zhang, Mid-infrared optoelectronic devices based on two-dimensional materials beyond graphene: status and trends, Nanomaterials 12 (13) (2022) 2260.
[24] S. Gao, N. Wang, S. Li, D. Li, Z. Cui, G. Yue, J. Liu, X. Zhao, L. Jiang, Y. Zhao, A multi-wall Sn/SnO_2@ carbon hollow nanofiber anode material for high-rate and long-life lithium-ion batteries, Angew. Chem. Int. Ed. 59 (6) (2020) 2465–2472.
[25] G. Li, S. Guo, B. Xiang, S. Mei, Y. Zheng, X. Zhang, B. Gao, P.K. Chu, K. Huo, Recent advances and perspectives of microsized alloying-type porous anode materials in high-performance Li-and Na-ion batteries, Energy Mater. 2 (2022) 200020.
[26] A. Hashemi, H.-P. Komsa, M. Puska, A.V. Krasheninnikov, Vibrational properties of metal phosphorus trichalcogenides from first-principles calculations, J. Phys. Chem. C 121 (48) (2017) 27207–27217.
[27] K.-Z. Du, X.-Z. Wang, Y. Liu, P. Hu, M.I.B. Utama, C.K. Gan, Q. Xiong, C. Kloc, Weak van der Waals stacking, wide-range band gap, and Raman study on ultrathin layers of metal phosphorus trichalcogenides, ACS Nano 10 (2) (2016) 1738–1743.
[28] Y. Ma, X. Lian, N. Xu, H. Jiang, L. Li, D. Zhang, G. Hu, S. Peng, Rational design of few-layer FePS3 nanosheets@ N-doped carbon composites as anodes for sodium-ion batteries, Chem. Eng. J. 427 (2022) 130882.
[29] X. Yang, Y. Luo, J. Li, H. Wang, Y. Song, J. Li, Z. Guo, Tuning mixed electronic/ionic conductivity of 2D CdPS3 nanosheets as an anode material by synergistic intercalation and vacancy engineering, Adv. Funct. Mater. 32 (2022) 2112169.
[30] A. Borenstein, O. Hanna, R. Attias, S. Luski, T. Brousse, D. Aurbach, Carbon-based composite materials for supercapacitor electrodes: a review, J. Mater. Chem. A 5 (25) (2017) 12653–12672.
[31] W. Qi, H. Zhao, Y. Wu, H. Zeng, T. Tao, C. Chen, C. Kuang, S. Zhou, Y. Huang, Facile synthesis of layer structured GeP3/C with stable chemical bonding for enhanced lithium-ion storage, Sci. Rep. 7 (2017) 1–7.
[32] Y. Zhao, X. Li, B. Yan, D. Li, S. Lawes, X. Sun, Significant impact of 2D graphene nanosheets on large volume change tin-based anodes in lithium-ion batteries: A review, J. Power Sources 274 (2015) 869–884.

[33] Y. Liu, H. Dai, L. Wu, W. Zhou, L. He, W. Wang, W. Yan, Q. Huang, L. Fu, Y. Wu, A large scalable and low-cost sulfur/nitrogen dual-doped hard carbon as the negative electrode material for high-performance potassium-ion batteries, Adv. Energy Mater. 9 (2019) 1901379.
[34] Y. Wang, Z. Wang, Y. Chen, H. Zhang, M. Yousaf, H. Wu, M. Zou, A. Cao, R.P. Han, Hyperporous sponge interconnected by hierarchical carbon nanotubes as a high-performance potassium-ion battery anode, Adv. Mater. 30 (2018) 1802074.
[35] M. Zheng, Y. Chi, Q. Hu, H. Tang, X. Jiang, L.i. Zhang, S. Zhang, H. Pang, Q. Xu, Carbon nanotube-based materials for lithium–sulfur batteries, J. Mater. Chem. A 7 (29) (2019) 17204–17241.
[36] S. Zhong, H. Liu, D. Wei, J. Hu, H. Zhang, H. Hou, M. Peng, G. Zhang, H. Duan, Long-aspect-ratio N-rich carbon nanotubes as anode material for sodium and lithium ion batteries, Chem. Eng. J. 395 (2020) 125054.
[37] S. Haghighat-Shishavan, M. Nazarian-Samani, M. Nazarian-Samani, S.H. Hosseini-Shokouh, T. Maschmeyer, K.-B. Kim, Realization of Sn2P2S6-carbon nanotube anode with high K+/Na+ storage performance via rational interface manipulation–induced shuttle-effect inhibition and self-healing, Chem. Eng. J. 435 (2022) 134965.
[38] H. Chen, R. Liu, Y. Wu, J. Cao, J. Chen, Y. Hou, Y. Guo, R. Khatoon, L. Chen, Q. Zhang, Interface coupling 2D/2D SnSe2/graphene heterostructure as long-cycle anode for all-climate lithium-ion battery, Chem. Eng. J. 407 (2021) 126973.
[39] X. Zhao, W. Cai, Y. Yang, X. Song, Z. Neale, H.-E. Wang, J. Sui, G. Cao, MoSe2 nanosheets perpendicularly grown on graphene with Mo–C bonding for sodium-ion capacitors, Nano Energy 47 (2018) 224–234.
[40] D.B. Schuepfer, F. Badaczewski, J.M. Guerra-Castro, D.M. Hofmann, C. Heiliger, B. Smarsly, P.J. Klar, Assessing the structural properties of graphitic and non-graphitic carbons by Raman spectroscopy, Carbon 161 (2020) 359–372.
[41] K. Yang, Q. Liu, Y. Zheng, H. Yin, S. Zhang, Y. Tang, Locally ordered graphitized carbon cathodes for high-capacity dual-ion batteries, Angew. Chem. Int. Ed. 60 (12) (2021) 6326–6332.
[42] B. Wang, F. Yuan, Q. Yu, W. Li, H. Sun, L. Zhang, D. Zhang, Q. Wang, F. Lai, W.A. Wang, Amorphous carbon/graphite coupled polyhedral microframe with fast electronic channel and enhanced ion storage for potassium ion batteries, Energy Stor. Mater. 38 (2021) 329–337.
[43] Z. Yi, J. Xu, Z. Xu, M. Zhang, Y. He, J. Bao, X. Zhou, Ultrafine SnSSe/multilayer graphene nanosheet nanocomposite as a high-performance anode material for potassium-ion half/full batteries, J. Energy Chem. 60 (2021) 241–248.
[44] Z. Han, F. Kong, J. Zheng, J. Chen, S. Tao, B. Qian, MnSe nanoparticles encapsulated into N-doped carbon fibers with a binder-free and free-standing structure for lithium ion batteries, Ceram. Int. 47 (1) (2021) 1429–1438.
[45] Y. Zhang, P. Chen, Q. Wang, Q. Wang, K. Zhu, K. Ye, G. Wang, D. Cao, J. Yan, Q. Zhang, High-capacity and kinetically accelerated lithium storage in MoO3 enabled by oxygen vacancies and heterostructure, Adv. Energy Mater. 11 (2021) 2101712.
[46] Q. Geng, H. Wang, J. Wang, J. Hong, W. Sun, Y. Wu, Y. Wang, Boosting the capacity of aqueous Li-Ion capacitors via pinpoint surgery in nanocoral-like covalent organic frameworks, Small Methods 6 (2022) 2200314.
[47] Q. Xu, H. Jiu, L. Zhang, W. Song, T. Gao, F. Guo, X. Li, H. Wei, C. Wang, Y. Liu, Rational design of 1D porous carbon microtubes supporting multi-size Bi2O3 nanoparticles for ultra-long cycle life lithium-ion battery anodes, ChemElectroChem 9 (2022) e202101321.
[48] Z. Hao, Q. Chen, W. Dai, Y. Ren, Y. Zhou, J. Yang, S. Xie, Y. Shen, J. Wu, W. Chen, Oxygen-deficient blue TiO2 for ultrastable and fast lithium storage, Adv. Energy Mater. 10 (2020) 1903107.
[49] Y. Fang, D. Luan, Y. Chen, S. Gao, X.W. Lou, Rationally designed three-layered Cu2S@ Carbon@ MoS2 hierarchical nanoboxes for efficient sodium storage, Angew. Chem. 132 (18) (2020) 7245–7250.
[50] L.L. Lu, Z.X. Zhu, T. Ma, T. Tian, H.X. Ju, X.X. Wang, J.L. Peng, H.B. Yao, S.H. Yu, Superior fast-charging lithium-ion batteries enabled by the high-speed solid-state lithium transport of an intermetallic Cu6Sn5 network, Adv. Mater. 34 (2022) 2202688.
[51] Y. Zhou, M. Zhang, Q.i. Wang, J. Yang, X. Luo, Y. Li, R. Du, X. Yan, X. Sun, C. Dong, X. Zhang, F. Jiang, Pseudocapacitance boosted N-doped carbon coated Fe7S8 nanoaggregates as promising anode materials for lithium and sodium storage, Nano Res. 13 (3) (2020) 691–700.
[52] H.u. Wu, S. Lu, S. Xu, J. Zhao, Y. Wang, C. Huang, A. Abdelkader, W.A. Wang, K. Xi, Y. Guo, S. Ding, G. Gao, R.V. Kumar, Blowing iron chalcogenides into two-dimensional flaky hybrids with superior cyclability and rate capability for potassium-ion batteries, ACS Nano 15 (2) (2021) 2506–2519.
[53] W. Xiao, X. Li, B. Cao, G. Huang, C. Xie, J. Qin, H. Yang, J. Wang, X. Sun, Constructing high-rate and long-life phosphorus/carbon anodes for potassium-ion batteries through rational nanoconfinement, Nano Energy 83 (2021) 105772.